# Supplementary Information

# Perovskite-type superlattices from lead-halide perovskite nanocubes

Ihor Cherniukh[1,2], Gabriele Rainò[1,2], Thilo Stöferle[3], Max Burian[4], Alex Travesset[5], Denys Naumenko[6], Heinz Amenitsch[6], Rolf Erni[7], Rainer F. Mahrt[3], Maryna I. Bodnarchuk[1,2], Maksym V. Kovalenko[1,2]*

[1]Department of Chemistry and Applied Bioscience, Institute of Inorganic Chemistry, ETH Zürich, Zürich, Switzerland.
[2]Laboratory of Thin Films and Photovoltaics, Empa — Swiss Federal Laboratories for Materials Science and Technology, Dübendorf, Switzerland.
[3]IBM Research Europe — Zürich, Rüschlikon, Switzerland.
[4]Swiss Light Source, Paul Scherrer Institut, Villigen PSI, Switzerland.
[5]Department of Physics and Astronomy, Iowa State University and Ames Lab, Ames, Iowa, USA.
[6]Institute of Inorganic Chemistry, Graz University of Technology, Graz, Austria.
[7]Electron Microscopy Center, Empa – Swiss Federal Laboratories for Materials Science and Technology, Dübendorf, Switzerland

**Supplementary Note 1. Calculation of packing densities**

**1.1. Methods and notations**

We consider mixed systems of spheres of diameter $d_s = 2r_s$ and cubes of edge length $l_c$. The case where the spheres are the larger (A-particles, $d_A = d_s$) and the cubes are the smaller particles (B-particles, $d_B = l_c$) $d_s > l_c$ is the main focus of this work. The packing fraction is the function of the effective size ratio, parameter $\gamma$, defined as

$$\gamma = \frac{d_B}{d_A} = \frac{l_c}{d_s} \leq 1 \quad \text{(S1)}$$

where $l_c$ is the edge length of the cube and $d_s$ is the diameter of sphere considered as hard cubes/spheres.

The general packing fraction will be denoted as

$$\eta^{i|j}(\gamma) \quad \text{(S2)}$$

where $i$, $j$ – $s$ or $c$. Thus, $\eta^{s|s}(\gamma)$ denotes the packing fraction of systems of hard spheres, $\eta^{s|c}(\gamma)$ - the packing fractions of spheres as A-particles and cubes as B-particles ($\gamma < 1$).

With cubes, there are additional degrees of freedom related to their orientation. The orientation of each cube will be denoted by the axis and angle of rotation[58]:

$$\text{Rotation parameters} = \{\vec{n}\ ,\ \Phi\} \quad \text{(S3)}$$

The lattice constants and packing fractions are calculated by HOODLT[59] as well as HOOMD[60] using rigid constrains[61] and the HPMC package[62].

**1.2. Lattices**

**1.2.1. NaCl**

From previous considerations[63], the packing fraction for the NaCl lattice [space group $Fm\bar{3}m$ (225), Wyckoff positions 2a, 2b] for an all-sphere case is

$$\eta^{s|s}(\gamma) = \begin{cases} \dfrac{\sqrt{2}\pi}{6}(1+\gamma^3) & \gamma < \gamma_{c,1} \\ \dfrac{2\pi}{3}\dfrac{1+\gamma^3}{(1+\gamma)^3} & \gamma \geq \gamma_{c,1} \end{cases} \quad \text{(S4)}$$

where $\gamma_{c,1} = \sqrt{2} - 1 \approx 0.4142$. The lattice constant is

$$a_L(\gamma) = \begin{cases} \sqrt{2}d_s & \gamma < \gamma_{c,1} \\ (1+\gamma)d_s & \gamma \geq \gamma_{c,1} \end{cases}. \quad \text{(S5)}$$

For B-particles cubes of edge $l_c = \gamma d_s$ oriented along the three primitive vectors, then the positions of the cube centers are the same as the corresponding inscribed spheres. Therefore, the only modification is that the packing fractions become

$$\eta^{s|c}(\gamma) = \eta^{s|s}(\gamma)\frac{\pi + 6\gamma^3}{\pi(1+\gamma^3)} \quad \text{(S6)}$$

while the lattice constant is still given by Eq. S5. The lattice consists of each A touching 12 other A for $\gamma < \gamma_c$ and each B with six A contacts along the faces of the B-cubes for the other case.

### 1.2.2. Binary $ABO_3$

The $ABO_3$ lattice is described by the space group *Pm*$\bar{3}$*m* (221) with a unit cell of one A particle in 1a, another B in 1b and three more O particles in positions 3c.

**All-sphere case**. For spherical B and O particles, we consider them fully equivalent (B = O). The packing fraction is

$$\eta^{s|s}(\gamma)=\begin{cases}\frac{\pi}{6}(1+4\gamma^3) & \gamma<\gamma_{c,1}\\ \frac{\pi\sqrt{2}}{3}\frac{1+4\gamma^3}{(1+\gamma)^3} & \gamma_{c,1}\le\gamma<\gamma_{c,2}\\ \frac{\pi}{48}\left(4+\frac{1}{\gamma^3}\right) & \gamma\ge\gamma_{c,2}\end{cases} \tag{S7}$$

with $\gamma_{c,1}=\sqrt{2}-1\approx 0.4142$ and $\gamma_{c,2}=1/(2\sqrt{2}-1)\approx 0.5469$. For $\gamma<\gamma_{c,1}$ each A particle has 6 A contacts, for $\gamma_{c,1}\le\gamma<\gamma_{c,2}$ each O particle has four contacts with an A particle, while A particles have 12, and finally, for $\gamma\ge\gamma_{c,2}$, each O particle has two contacts with each B particle and each B particle has 6 contacts with O particles.

The lattice constant is given by

$$a_L(\gamma)=\begin{cases}d_s & \gamma<\gamma_{c,1}\\ \frac{1+\gamma}{\sqrt{2}}d_s & \gamma_{c,1}\le\gamma<\gamma_{c,2}\\ 2\gamma d_s & \gamma\ge\gamma_{c,2}\end{cases}. \tag{S8}$$

Let us investigate the Orbifold topological model (OTM) branch for $\gamma>\gamma_{c,1}$. It consists of four vortices in the O particles, while the A particles remain vortex-free so that the six A-A contacts remain. Therefore, it is

$$\bar{\gamma}=\gamma_{c,1}. \tag{S9}$$

This relation remains valid until the B and O particles contact each other, which occurs for $\gamma\equiv\bar{\gamma}_{c,1}=0.5$, so that for $\bar{\gamma}_{c,1}\le\gamma<\gamma_{c,2}$ it is

$$\bar{\gamma}=2\sqrt{2}\gamma-1. \tag{S10}$$

Then, for $\gamma>\gamma_{c,2}$ another OTM branch exists where

$$\bar{\gamma}=\frac{1+\left(1-\sqrt{2}\right)\gamma}{\sqrt{2}} \tag{S11}$$

which applies until O particles have contacts among each other at $\gamma = 1$. Hence, the lattice constant of the OTM branch is given by

$$a_{L,OTM}(\gamma)=\begin{cases}d_s & \gamma<\bar{\gamma}_{c,1}\\ 2\gamma d_s & \bar{\gamma}_{c,1}\le\gamma<\gamma_{c,2}\\ \frac{1+\gamma}{\sqrt{2}}d_s & \gamma\ge\gamma_{c,2}\end{cases}. \tag{S12}$$

The packing fraction is

$$\eta_{OTM}^{s|s}(\gamma)=\begin{cases}\dfrac{\pi}{6}(1+4\gamma^3) & \gamma<\bar{\gamma}_{c,1}\\ \dfrac{\pi}{48}\left(4+\dfrac{1}{\gamma^3}\right) & \bar{\gamma}_{c,1}\le\gamma<\gamma_{c,2}\\ \dfrac{\pi\sqrt{2}}{3}\dfrac{1+4\gamma^3}{(1+\gamma)^3} & \gamma\ge\gamma_{c,2}\end{cases}. \quad \text{(S13)}$$

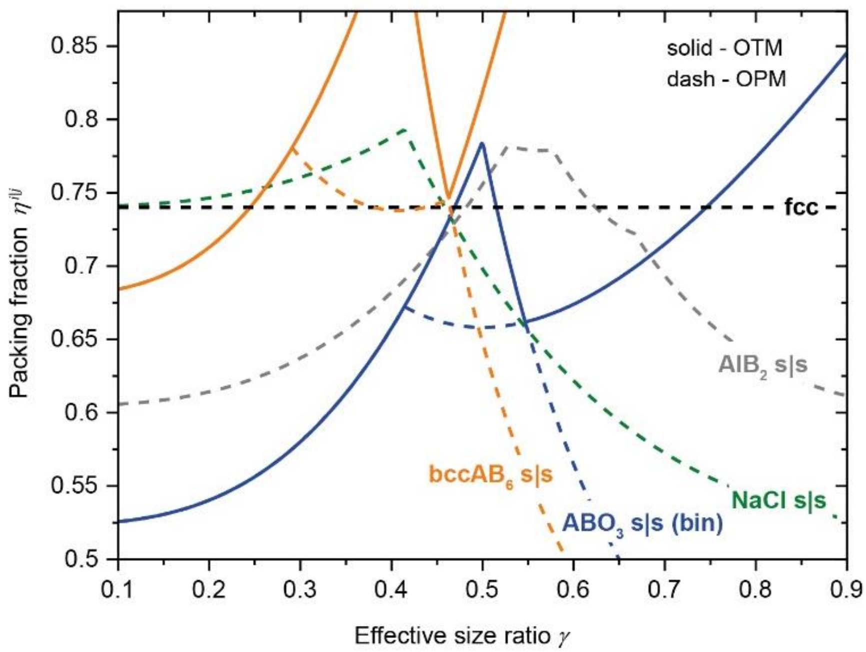


**Supplementary Fig. 1 | Packing fractions for the four different lattices considered, assembled from spherical particles.**

Note that at $\gamma = 0.5$, $ABO_3$-type lattice packing density ($\eta_{OTM}^{s|s}(0.5)\approx 0.7854$, Supplementary Fig. 1) may exceed that of two competing phases, $AlB_2$ and NaCl, but is lower than that of $bccAB_6$ (or $CaB_6$) phases[63], which are usually found experimentally[64]. Even after neglecting $bccAB_6$, the formation of $ABO_3$ would be expected only over a very narrow $\gamma$-range and, because this is only the OTM branch that has such high density, reaching these packing densities requires compression of the nanocrystal (NC) radius $r_B$ to $\bar{r}_B = 2\gamma_{c,1}r_B \approx 0.8284 r_B$. This is a very significant compression that requires long ligands and/or small cores. In addition, such compression is difficult to realize for isotropic spherical NCs, unlike to cubes and other sharper shapes, which favour significant ligand bending in specific mutual geometries. On contrary, when switching to cubes as B/O-type NCs, the packing fraction for the $ABO_3$ (within OTM, as discussed below and shown in Fig. 1k of the Main Text) is high over a broader range of $\gamma$, and with compressions that are easily realizable.

**The case of cubes as B/O-particles.** For B- and O-cubes of the same size, and in agreement with the observed electron diffraction, the positions and orientations (as described in Eq. S3) are given by

| Wyckoff | Coordinate | $\vec{n}$ | Φ |
|---|---|---|---|
| 3c | $\left(\left(\frac{1}{2},\frac{1}{2},0\right)a_L\right)$ | (0, 0, 1) | $\frac{\pi}{4}$ |
| 3c | $\left(\frac{1}{2},0,\frac{1}{2}\right)a_L$ | (0, 1, 0) | $\frac{\pi}{4}$ |
| 3c | $\left(0,\frac{1}{2},\frac{1}{2}\right)a_L$ | (1, 0, 0) | $\frac{\pi}{4}$ |
| 1b | $\left(\frac{1}{2},\frac{1}{2},\frac{1}{2}\right)a_L$ | (0, 0, 0) | 0 |

(S14)

Then, for $\gamma < \gamma_{c,1}$, the cubes are rattlers and the lattice constant is defined by the A-hard spheres. For $\gamma \geq \gamma_{c,1}$, the optimal lattice constant corresponds to the 3c cubes having contacts at each of their vertices, with a packing fraction

$$\eta^{s|c}(\gamma) = \begin{cases} \frac{\pi}{6}\left(1+\frac{24}{\pi}\gamma^3\right) & \gamma < \gamma_{c,1} \\ \frac{\pi(5\sqrt{2}-7)}{6}\left(\frac{24}{\pi}+\frac{1}{\gamma^3}\right) & \gamma \geq \gamma_{c,1} \end{cases} \tag{S15}$$

with lattice constant

$$a_L(\gamma) = \begin{cases} d_s & \gamma < \gamma_{c,1} \\ \frac{\gamma}{\sqrt{2}-1}d_s & \gamma \geq \gamma_{c,1} \end{cases}. \tag{S16}$$

This solution consists of each A with 6 A contacts for $\gamma < \gamma_{c,1}$ and each 3c O-cube touching 8 other O-cubes at the vertices for $\gamma \geq \gamma_{c,1}$.

### 1.3. Theoretical and experimental lattice constants

#### 1.3.1. Lattice constants within hard sphere/cubes model

The hard-sphere diameter $d_S$ of a spherical NC[63,65,66] is given by the optimal packing model (OPM) formula[67]

$$\frac{d_s}{d_{core}} \equiv \tau = (1+3\lambda\xi)^{1/3} \tag{S17}$$

in which $\lambda = \frac{2L}{d_{core}}$ is the softness of the NC, where $L$ is the maximum stretched length of the ligand, and $\xi = \frac{\sigma}{\sigma_{Max}}$, where $\sigma_{Max}$ is the largest possible grafting density.

The hard-sphere effective diameter depends on the maximum grafting density $\sigma_{Max}$, which depends on the core diameter[66]. For core diameters $d_s < 5$ nm these maximum grafting densities may be significantly enhanced by the curvature, but the NCs in the current experiment are much larger; therefore, we will use the large diameter value of $\sigma_{Max} \approx 4.7\ \mathrm{nm}^{-2}$ for our calculations. The grafting densities of didodecyldimethylammonium (DDAB, 0.81 nm$^{-2}$ for $CsPbBr_3$ NCs) and oleic acid (4.4 nm$^{-2}$ for $Fe_3O_4$ and

$NaGdF_4$) were derived from thermogravimetric analysis and from Ref.[68] and were consistent with interparticle separation in single-component superlattices (SLs). The maximum extension length ($L$ = 2.29 nm) for oleic acid was calculated as described in Ref.[63].

The grafting density for the cubes is relatively low. For example, under the assumption that DDAB may be represented as two hydrocarbon chains, then $\sigma_{Max} \approx 4.7/2 = 2.35$ nm$^{-2}$. The hard cube is therefore defined by an edge $l_c$

$$l_c = l_{core} + 2\frac{\sigma}{\sigma_{Max}} L \approx l_{core} + 1.12 \text{ (in nm)} \tag{S18}$$

where it has been assumed that the hydrocarbons are space-filling within their footprint area, that is, without any splay, which is the same assumption that leads to the OPM formula Eq. S17 defining the hard-sphere diameter for the spherical NCs. For the maximum extension length, we use the formula $L = 0.122(n+1)$ (see Ref.[63] for further discussion), with $n = 13$ (there are 12 carbons on each side chain of DDAB, and 1 more carbon is included to account for the two additional methyl groups attached to the nitrogen).

The results for the softness parameters and hard-sphere effective diameters $\boldsymbol{d_S}$ are shown in Supplementary Table 1 for all NC samples used in this work, along with hard-cube edge length ($\boldsymbol{l_c}$) for cubes. One can then compute the parameter $\gamma$, defined in Eq. S1 and shown in Supplementary Table 2 for each binary SL. Then, the lattice constants are calculated from the formulas (Eq. S5 and S16) described above and, in Supplementary Table 2, are compared to the experimental lattice parameters derived from TEM images and GISAXS measurements.

One should note that the theoretical results are pure predictions that do not include any fitting parameters. The discrepancy with experiments is at most of a few Å, which, given the uncertainties in terms of core radius or even lattice constant (when not measured by X-ray), is an excellent agreement. The only exception occurs for the $ABO_3$ SL for $\gamma > \gamma_{c,1}$. As is evident from the Main Text Fig. 1k, these values of $\gamma$ correspond to low < 0.5 packing fractions, which indicates that some of the NCs are not accurately represented by hard spheres or cubes and require the considerations of ligand textures[63,65], *i.e.* "vortices", as discussed below with the OTM model.

### 1.3.2. Orbifold topological model for spheres/cubes $ABO_3$-type binary SL

The calculation of the hard-cube edge Eq. S18 assumes that ligands form a maximally dense flat brush, so it becomes exact for very large cubes, namely, when $l_{core} >> \frac{\sigma}{\sigma_{Max}} L \approx 1$. Even if these conditions are not strictly satisfied, Eq. S18 remains a good approximation if the lattice constant is determined by cubes interacting through their faces or with spherical NCs. However, in the $ABO_3$ lattice for $\gamma \geq \gamma_{c,1}$, see Eq. S7, the cubes interact through their vertices, and therefore, there is the possibility of ligand textures that bend away from the cube faces, enabling a denser packing, similarly as reported for spherical NCs whenever vortices[63,65] are allowed (see Supplementary Fig. 2).

Because the ligand texture deformations are along the corners, we define a modified effective size ratio

$$\bar{\gamma} = \frac{\bar{l}_c}{d_s} \tag{S19}$$

where $\bar{l}_c < l_c$ is the deformed cube edge as determined by the cube corners. The lattice constant is given by Eq. S16, hence

$$a_{L,OTM}(\bar{\gamma}) = \frac{\bar{\gamma}}{\sqrt{2}-1} d_s \,. \tag{S20}$$

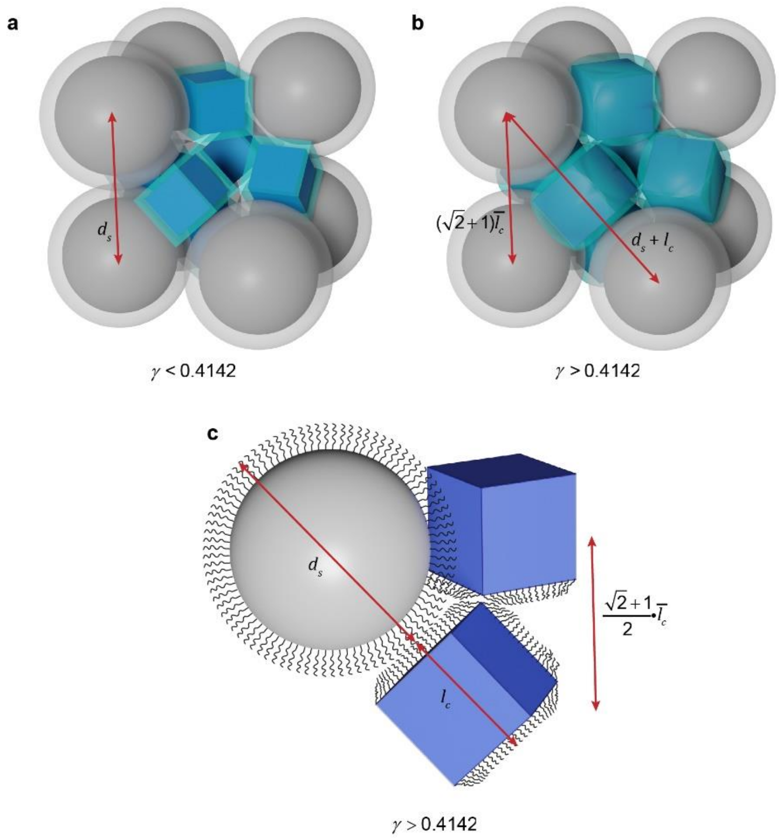


**Supplementary Fig. 2 | Representation of the ligand shell around NCs in binary $ABO_3$ lattice according to hard sphere/cube (a, $\gamma < \gamma_{c,1}$) and OTM (b and c, $\gamma > \gamma_{c,1}$) models.**

The fundamental equation is then obtained by imposing that all 3c cubes are in contact with the spherical NCs in the 1a positions. Note that because these contacts are determined by $l_c$ (as opposed to $\bar{l}_c$), since they cannot be deformed. Thus we obtain for A-B distance (A and B in contact, corresponding to the distance between Wyckoff positions 1a and 3c):

$$\frac{1+\gamma}{2} d_s = \frac{\bar{\gamma}}{\sqrt{2}-1} \frac{\sqrt{2}}{2} d_s \tag{S21}$$

leading to OTM formula for the lattice constant:

$$a_{L,OTM}(\gamma) = \frac{1+\gamma}{\sqrt{2}} d_s \qquad \gamma_{c,1} \le \gamma < \bar{\gamma}_{c,2}\,. \tag{S22}$$

This formula is valid provided that the two conditions

$$\bar{\gamma} \ge \frac{l_{core}}{d_s} = \bar{\gamma}_{\min} \tag{S23}$$

($\bar{\gamma}$ must be higher than minimum value $\bar{\gamma}_{\min}$ of 3c cube cores touching at vertices)

$$\frac{\bar{\gamma}}{2(\sqrt{2}-1)} \ge \gamma \tag{S24}$$

(distance between 1b and 3c ≥ $l_c$, minimum distance between two cubes)

Since $\bar{\gamma}_{\min}$ is a function of both the $l_{core}$ and the NC hard-sphere diameter, it may be expressed as

$$\bar{\gamma}_{\min} = \frac{l_{core}}{l_c}\gamma \equiv r\gamma \tag{S25}$$

where $r$ is a constant for a cube of fixed core and ligands.

The limit $\bar{\gamma}_{c,2}$ where Eq. S22 applies is obtained from Eq. S23 combined with Eq. S20:

$$\bar{\gamma}_{c,2} = \frac{1}{\frac{\sqrt{2}}{\sqrt{2}-1}r-1} \overset{r=0.8848}{\approx} 0.4948 \tag{S26}$$

where $r = \frac{8.6}{8.6+1.12} = 0.8848$ corresponds to the cubes in the $ABO_3$ experiment. Alternatively, from Eq. S24 combined with Eq. S20 one receives

$$\bar{\gamma}_{c,2} = \frac{1}{2\sqrt{2}-1} \approx 0.5469\,. \tag{S27}$$

Therefore, $\bar{\gamma}_{c,2}$ is given by Eq. S26 provided that

$$r \geq r_{crit} \equiv 2(\sqrt{2}-1) \approx 0.8284 \tag{S28}$$

and by Eq. S27 if $r < r_{crit}$.

The lattice constant for $\gamma \geq \bar{\gamma}_{c,2}$ is given as

$$a_{L,OTM}(\gamma) = \begin{cases} (\sqrt{2}+1)r\gamma d_s & r \geq r_{crit} \\ 2\gamma d_s & r < r_{crit} \end{cases}\,. \tag{S29}$$

The packing fraction is given by

$$\eta^{s|c}_{OTM}(\gamma) = \begin{cases} \frac{\pi}{6}\left(1+\frac{24}{\pi}\gamma^3\right) & \gamma < \gamma_{c,1} \\ \frac{\sqrt{2}\pi}{3(1+\gamma)^3}\left(1+\frac{24}{\pi}\gamma^3\right) & \gamma_{c,1} \leq \gamma < \bar{\gamma}_{c,2} \\ \frac{\pi}{6(\sqrt{2}+1)^3\gamma^3 r^3}\left(1+\frac{24}{\pi}\gamma^3\right) & \gamma \geq \bar{\gamma}_{c,2} \end{cases}\,. \tag{S30}$$

Note that if $r \leq r_{crit}$, then one must take $r = r_{crit}$ in Eq. S30. Results are shown in Fig. 1k of the Main Text. Clearly, $\gamma > \gamma_{c,1}$ (0.4142) packing density in OTM model greatly exceeds a purely hard-sphere/hard-cube approximation for $ABO_3$ structure. The OTM-corrected values for lattice constants now show much better agreement with the experimental values (Supplementary Table 2, last column).

**Supplementary Table 1. List of NCs and their properties.** The parameter $\lambda$ is defined in Eq. S17. $d_s$ is the hard-sphere diameter, $l_c$ the hard-cube edge length.

| Core | $d_{core}$ (nm) | $\lambda$ | $d_s$ or $l_c$ (nm) |
|---|---|---|---|
| **$CsPbBr_3$** | 5.3(4) | 0.626 | 6.42 |
| | 8.6(5) | 0.386 | 9.72 |
| **$Fe_3O_4$** | 10.2(6) | 0.449 | 13.39 |
| | 12.5(7) | 0.366 | 15.87 |
| | 14.5(6) | 0.316 | 17.97 |
| | 14.7(5) | 0.312 | 18.18 |
| | 15.6(7) | 0.294 | 19.11 |
| | 16.8(9) | 0.273 | 20.36 |
| | 19.5(9) | 0.235 | 23.14 |
| | 19.8(10) | 0.231 | 23.45 |
| | 20.7(1.1) | 0.221 | 24.37 |
| | 21.5(1.4) | 0.213 | 25.14 |
| | 25.1(1.4) | 0.182 | 28.81 |
| **$NaGdF_4$** | 16.5(9) | 0.278 | 20.00 |

**Supplementary Table 2. Summary of the structural parameters for the obtained SLs.** The last three columns represent calculated lattice parameters ($a_L$) based on hard-sphere and hard cube model, their experimental values ($a_{exp}$) obtained from TEM images and also GISAXS(*****) and the lattice parameters calculated with OTM approximation ($a_{L,OTM}$).

| Structure | $CsPbBr_3$ $l_{core}$ (nm) | $CsPbBr_3$ $l_c$ (nm) | $Fe_3O_4$ $d_{core}$ (nm) | $Fe_3O_4$ $d_{HS}$ (nm) | $\gamma$ | $a_L$ (nm) | $a_{exp}$ (nm) | $a_{L,OTM}$ (nm) |
|---|---|---|---|---|---|---|---|---|
| Binary $ABO_3$ | 8.6(5) | 9.72 | 14.5(6) | 17.97 | 0.541 | 23.47 | 20.5* | 20.77 |
| | 8.6(5) | 9.72 | 15.6(7) | 19.11 | 0.509 | 23.48 | 20.7 | 20.78 |
| | 8.6(5) | 9.72 | 16.5(9) $NaGdF_4$ | 20.00 | 0.486 | 23.47 | 21.6 | 21.02 |
| | 8.6(5) | 9.72 | 16.8(9) | 20.36 | 0.477 | 23.45 | 21.8 | 21.26 |
| | 8.6(5) | 9.72 | 19.5(9) | 23.14 | 0.420 | 23.46 | 23.5* | 23.23 |
| | 8.6(5) | 9.72 | 20.7(1.1) | 24.37 | 0.399 | 24.37 | 24.4 | 24.37 |
| NaCl | 8.6(5) | 9.72 | 15.6(7) | 19.11 | 0.507 | 28.83 | 28.5 | 28.83 |
| | 8.6(5) | 9.72 | 19.8(1.0) | 23.45 | 0.414 | 33.16 | 33.6 | 33.16 |
| | 8.6(5) | 9.72 | 25.1(1.4) | 28.81 | 0.337 | 40.74 | 40.9 | 40.74 |
| | 5.3(4) | 6.42 | 14.7(5) | 18.18 | 0.353 | 25.7 | 25.3 | 25.7 |
| | 5.3(4) | 6.42 | 15.6(7) | 19.11 | 0.336 | 27.0 | 27.0 | 27.0 |
| | 5.3(4) | 6.42 | 19.8(1) | 23.45 | 0.274 | 33.2 | 32.9 | 33.2 |

**Supplementary Note 2. Relationship between crystallographic lattice planes and facets in $CsPbBr_3$ nanocubes**

$CsPbBr_3$ NCs crystallize in perovskite orthorhombic *Pnma* structure, which can be derived from the ideal perovskite cubic $Pm\bar{3}m$ structure (which consists of 3D network of corner-sharing $PbBr_6$ octahedra and Cs occupying cuboctahedral voids) by a small octahedral tilting. The relationship between cubic and orthorhombic unit cells is shown in the figure below: the orthorhombic cell axis $\mathbf{b_{orth}}$ is parallel to cubic cell axis $\mathbf{b_c}$, $\mathbf{a_{orth}}$ aligns to ($\mathbf{a_c}$ + $\mathbf{c_c}$) and $\mathbf{c_{orth}}$ aligns to ($\mathbf{c_c}$ - $\mathbf{a_c}$). Due to these relationships the orthorhombic lattice parameters $a_{orth}$ and $c_{orth}$ are almost identical: $a_{orth}$ = 8.2502 Å ≈ $\sqrt{2}a_c$, $c_{orth}$ = 8.2035 Å ≈ $\sqrt{2}a_c$ and $b_{orth}$ = 11.7532 Å ≈ $2a_c$[69].

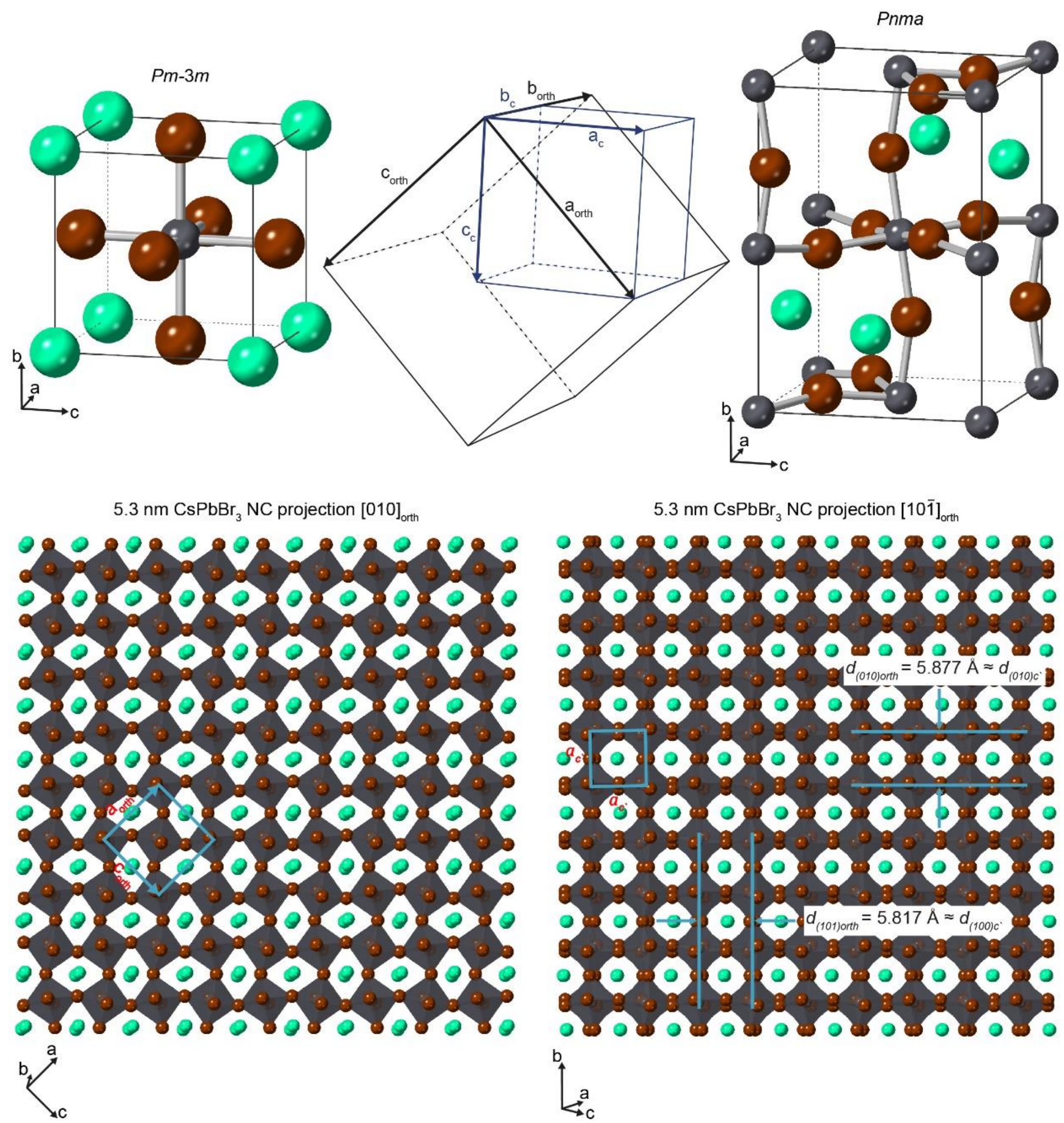


**Supplementary Fig. 3 | Relationship between crystallographic lattice planes and facets in $CsPbBr_3$ nanocubes.**

$CsPbBr_3$ NCs are terminated by two {010} and four {101} lattice planes. Because the difference between {010} and {101} d-spacings is only 1.0% and not readily detectable by conventional electron diffraction (ED) we, for the sake of simplicity, assign ED reflections of $CsPbBr_3$ as originated from pseudocubic structure with lattice constant $a_{c`} \approx 5.85$ Å and adopt the notation [100], [010] and [001] referring to $\mathbf{a}_{c`}$, $\mathbf{b}_{c`}$ and $\mathbf{c}_{c`}$ cubic crystallographic axes[70,71].

Given the small structural difference between all {100} lattice planes and natural propensity of lead cation to complete octahedral coordination, all six facets of $CsPbBr_3$ NCs tend to be AX'-terminated (where A – $Cs^+$, oleylamonium, didodecyldimethylammonium, X' – $Br^-$, oleate). Consequently, the growth of all {100} lattice planes in six directions is similar and exceeds the growth in other directions, which makes the non-truncated cubic shape the most stable for lead halide perovskites[72], contrary to other cubic NCs, for instance, cubic lead sulfide, which vertices and edges are bevelled by (111) and (110) lattice planes, respectively[73,74].

## Supplementary Note 3. GISAXS characterization of SLs

Indexing of the binary SL peaks was done manually for the case of a grazing incidence geometry (noted by white markers in Supplementary Fig. 4 and 7f). Here, X-rays are scattered by the binary SLs either prior to or subsequent to refraction with the sample substrate. As scattering images were taken at low incidence angles of 0.04°, we also have to account for a partial scattering contribution stemming from (Laue-type) transmission-diffraction (noted by red markers in Supplementary Fig. 4 and 7f). Here, Laue-type diffraction occurs if X-rays are scattered directly by the binary SLs and are not refracted by the sample substrate.

Scattering images of the $ABO_3$-type binary SL comprising 8.6 nm $CsPbBr_3$ and 19.5 nm $Fe_3O_4$ NCs ($\gamma = 0.420$) on silicon nitride membrane show a regular and highly symmetric scattering pattern (see Fig. 1c from the Main Text). All reflections can be indexed using a simple-cubic ($Pm\bar{3}m$) symmetry with 24.2 nm unit cell dimension (see Supplementary Fig. 4a). Here, we do not observe the absence of any distinct peak families, which would be a characteristic sign of a higher symmetry packing. Note that $CsPbBr_3$ and $Fe_3O_4$ have different mean electron density and hence different scattering length contrast in the X-ray scattering measurement. An e.g. body-centered cubic (bcc) structural motif, where $Fe_3O_4$ NCs occupy corner points and $CsPbBr_3$ NCs reside at the body-centered position, would hence still give the scattering pattern of a simple cubic motif where only the (phase-terms determining) relative peak intensities are affected. Furthermore, assuming a bcc arrangement of $Fe_3O_4$ NCs, intercalation of $CsPbBr_3$ NCs with site-dependent orientation would break the bcc symmetry such that only the simple-cubic motif remains.

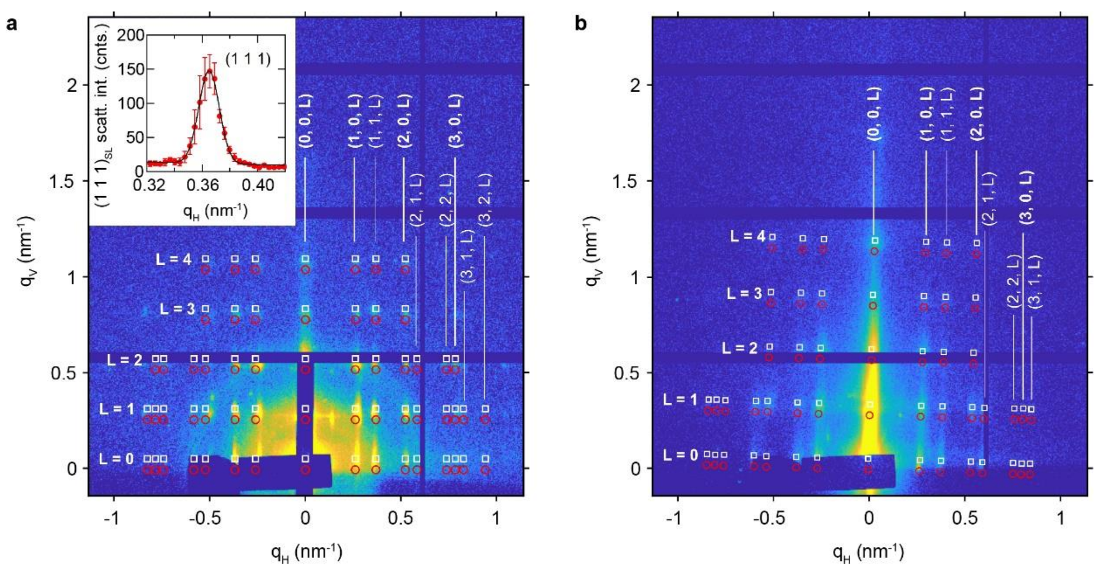


**Supplementary Fig. 4 | Indexing of GISAXS scattering images from $ABO_3$-type binary SL comprising 8.6 nm $CsPbBr_3$ and 19.5 nm $Fe_3O_4$ NCs. a**, The binary SL self-assembled on a silicon nitride membrane corresponds to an undistorted cubic lattice with $a = b = c = 24.2$ nm. The inset shows the Gaussian peak fit (FWHM = 0.0174 $nm^{-1}$) of an in-plane cut (average over $n = 10$ pixels, corresponding to $\Delta q_v = 0.02$ $nm^{-1}$) through the (1, 1, 1) reflection to determine the coherent in-plane domain size of the binary SL (error bars denote the standard-deviation of the scattering intensity along $q_v$ over $n = 10$ pixels within the horizontal cut). **b**, The scattering image of the same system self-assembled on a TEM grid can only be indexed using an out-of-plane compressed tetragonal unit cell. White markers correspond to the grazing-incidence diffraction-peak positions and red markers show the corresponding Laue-type diffraction pattern.

To quantify the degree of crystalline order, we determine the size of the coherent scattering volume, which is directly related to the crystalline domain size. Following the Scherrer equation, we determine the peak width (FWHM) of the isolated $(1\ 1\ 1)_{SL}$ reflection (which is not distorted by any other diffuse scattering contribution) with $\Delta q$ = 0.0174 $nm^{-1}$, which corresponds to a mean in-plane domain size of $2\pi/\Delta q \approx$ 361 nm.

The same $ABO_3$-type binary SL comprising 8.6 nm $CsPbBr_3$ and 19.5 nm $Fe_3O_4$ NCs ($\gamma$ = 0.420) was also self-assembled on a TEM grid. Here, the GISAXS scattering pattern can only be indexed using a tetragonal geometry (*P*4/*mmm*), with slight out-of-plane compression [$a = b$ = 23.5 nm; $c$ = 22.0 nm] – see Supplementary Fig. 4b. This out-of-plane lattice compression is likely a side effect of the solvent-evaporation procedure, creating an anisotropic concentration gradient and hence uniaxial thermodynamic pressure. Indeed, the same effect is known to occur in binary SL of classical spherical NCs[75].

## Supplementary Note 4. Superfluorescence in various binary superlattices

We have assembled $ABO_3$-type SLs of 8.6 nm $CsPbBr_3$ NCs with differently sized $NaGdF_4$ NCs (15.2 nm and 19.5 nm), and compared their optical properties with a NaCl-type SL formed by the assembly of 8.6 nm $CsPbBr_3$ NCs and 18.6 nm $NaGdF_4$ NCs by performing ultrafast optical spectroscopy at cryogenic temperatures. These samples were ideally suited for such a comparison as they were phase-pure; that is, where only a specific SL ($ABO_3$ or NaCl) is found macroscopically across the entire sample, without a substantial amount of disordered regions or other phases (both single-component and binary). We have found that SF is absent in NaCl-type SLs, while two $ABO_3$-type SLs clearly exhibit the typical burst emission of SF of two different kinds, namely blue and red-shifted with respect to excitonic PL, as discussed below and illustrated in Supplementary Fig. 23.

In addition to the different arrangements of the emitting dipoles, the drastic difference between $ABO_3$- and NaCl-type SLs in achieving SF can be due to the much lower effective NC density in NaCl-type SLs ($CsPbBr_3$ NCs concentration of $1.18 \times 10^5$ $\mu m^{-3}$, perovskite NC volume fraction of 0.0748), which are characterized by a 1:1 ratio between emitting perovskite NCs and $NaGdF_4$ NCs. In $ABO_3$-type SLs (4:1 ratio), the higher perovskite NC density ($4.58 \times 10^5$ $\mu m^{-3}$, perovskite NC volume fraction of 0.291) and the much reduced NC-to-NC distance can facilitate the occurrence of coherent coupling. In fact, NaCl-type SLs only show the characteristic emission from neutral excitons and trions (Supplementary Fig. 23a), while the radiative rates remain almost unchanged for higher fluences (Supplementary Fig. 23b, c). On the contrary, $ABO_3$-type SLs clearly show a significant shorting of the radiative lifetime down to few picoseconds with the appearance of oscillations in the time domain (Supplementary Fig. 23e, f). Furthermore, by exploring $ABO_3$-type SLs composed of large, 19.5 nm $NaGdF_4$ NCs ($3.16 \times 10^5$ $\mu m^{-3}$, perovskite NC volume fraction of 0.201), we found that SF can occur almost resonantly (actually, somewhat blue-shifted) with the exciton transition (Supplementary Fig.23 g-i), unlike to a red-shifted SF in the case of smaller $NaGdF_4$ NCs. We have two hypotheses for this different SF behaviour. One possibility is that since almost an order of magnitude higher fluence is required for its occurrence (Supplementary Fig. 23g-i), we believe that this could be due to SF from biexcitons, as reported for CuCl QDs embedded in a NaCl matrix[76]. Having increased the perovskite NC-to-NC distance by employing larger $NaGdF_4$ NCs, the coherent coupling among several NCs could be reduced in the single exciton regime but still occurs through the interaction of biexcitons, given their higher oscillator strength. Recent experiments which combine fluence-dependent transient absorption spectroscopy with a robust spectral deconvolution method unveiled the repulsive character of exciton-exciton interactions in $CsPbBr_3$ NCs[77], which would be in line with our observations of a small blue-shift. However, fluence-dependent experiments do not show the typical power-law behavior expected for biexcitons (power-law exponent of 2), suggesting that the Auger process might alter the dynamics. Alternatively, a second hypothesis is that SF still emerges from single excitons where the NCs are heated by the strong excitation pulse to emit at slightly higher energy (as also observed for the non-SF NaCl-type SLs). The increased fluence onset can then be related to the increased energetic disorder present at higher energy due to quantum confinement.

**Supplementary Figures 5-14**

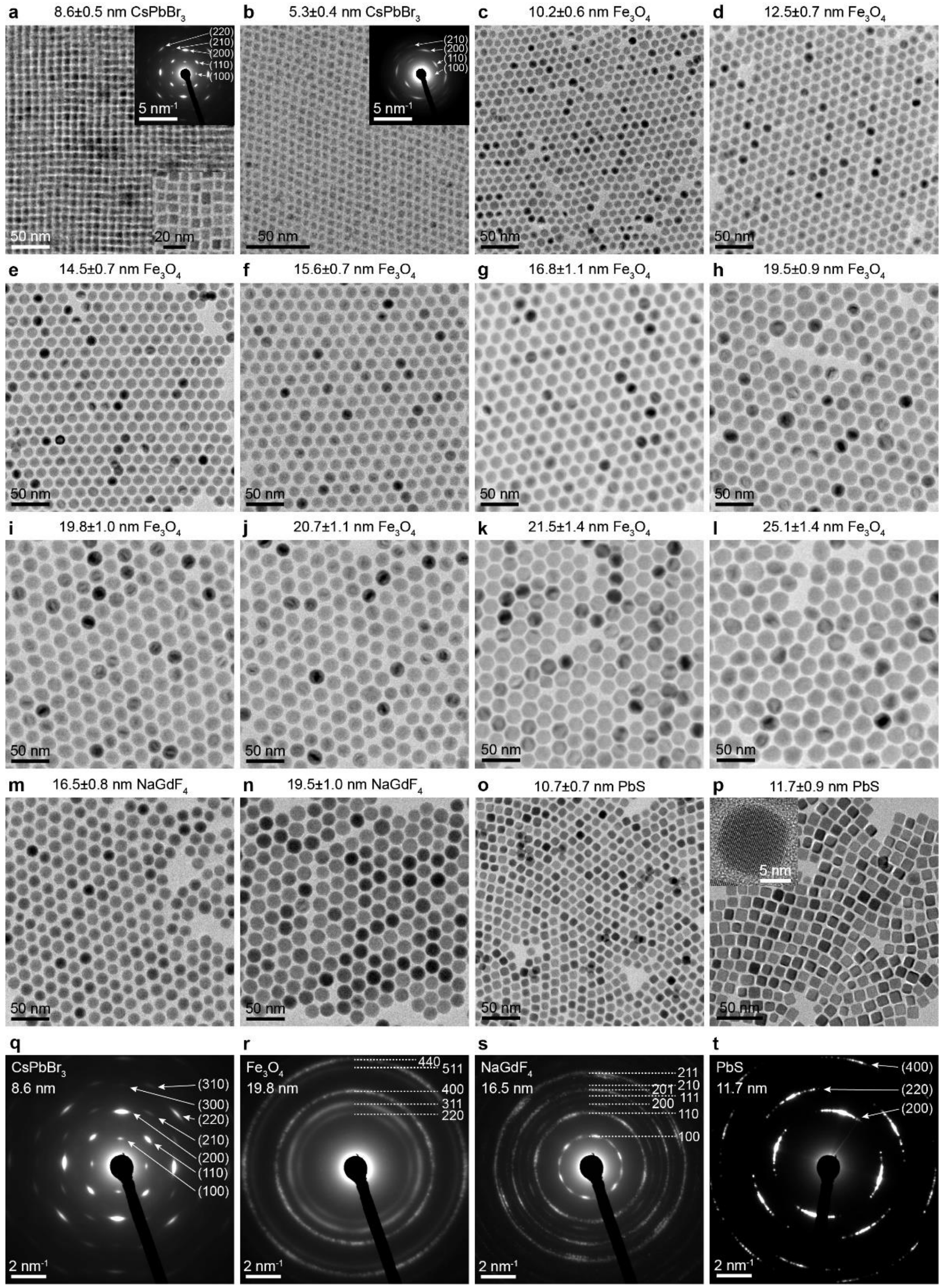


**Supplementary Fig. 5 | TEM images and ED patterns of monodisperse NC building blocks used for self-assembly. a**, **b**, DDAB-treated $CsPbBr_3$ NCs. **c**-**l**, oleate-capped $Fe_3O_4$ NCs. **m**, **n**, oleate-capped $NaGdF_4$ NCs. **o**, **p**, oleate-capped PbS NCs. **q**-**t**, Corresponding selected area wide-angle electron diffraction (ED) patterns of these NCs. NC size-distribution was in the range from 4.2 to 7.5% (standard size deviation) and was calculated based on 300 particles. ED patterns of $CsPbBr_3$ NCs confirm perovskite phase. The presence of diffraction spots, instead of continuous powder rings, indicates the consistency of NCs orientation and the alignment of <100> crystallographic directions of nanocubes with the [001] zone axis parallel to an electron beam.

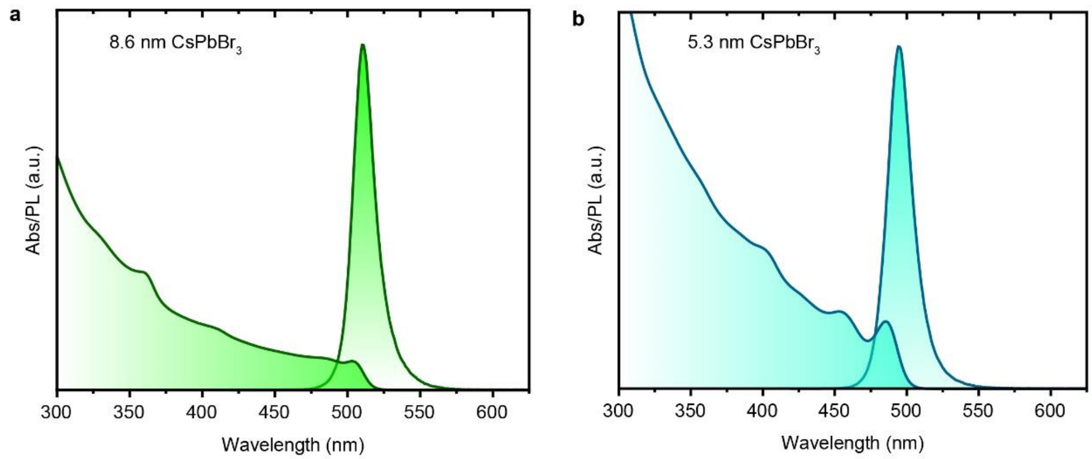


**Supplementary Fig. 6 | Optical properties of colloidal $CsPbBr_3$ NCs dispersed in toluene. a**, Absorption and PL spectra of 8.6 nm $CsPbBr_3$ NCs (PL quantum yield > 90%). **b**, Absorption and PL spectra of 5.3 nm $CsPbBr_3$ NCs (PL quantum yield > 55%).

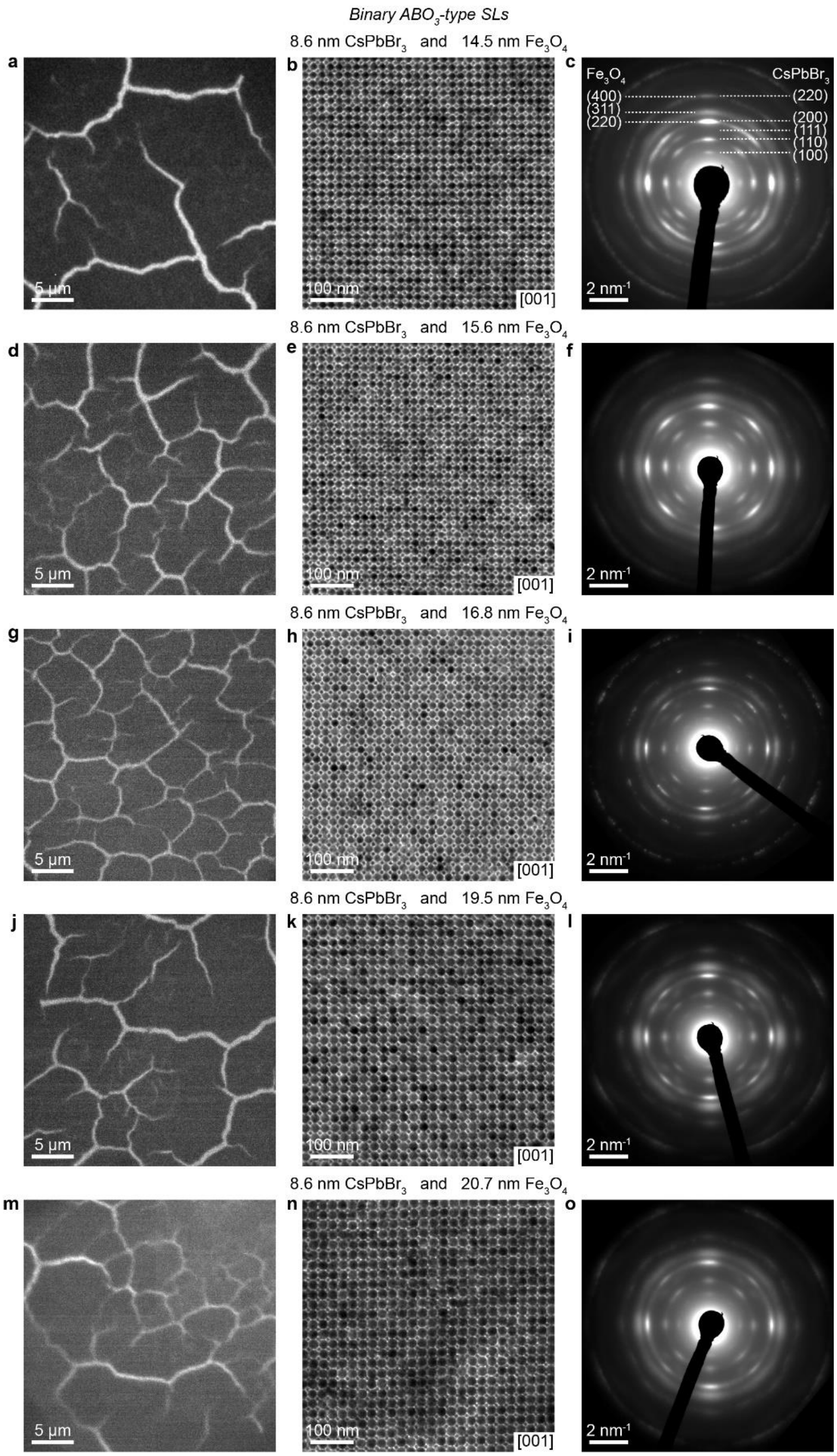


**Supplementary Fig. 7 | Binary $ABO_3$-type SLs comprising 8.6 nm $CsPbBr_3$ NCs and differently sized spherical $Fe_3O_4$ NCs (14.5-20.7 nm).** **a**-**c**, $\gamma = 0.541$. **d**-**f**, $\gamma = 0.509$. **g**-**i**, $\gamma = 0.486$. **j**-**l**, $\gamma = 0.420$. **m-o**, $\gamma = 0.399$. Distinct ED reflections from B- and O-positioned $CsPbBr_3$ NCs are maintained across all samples.

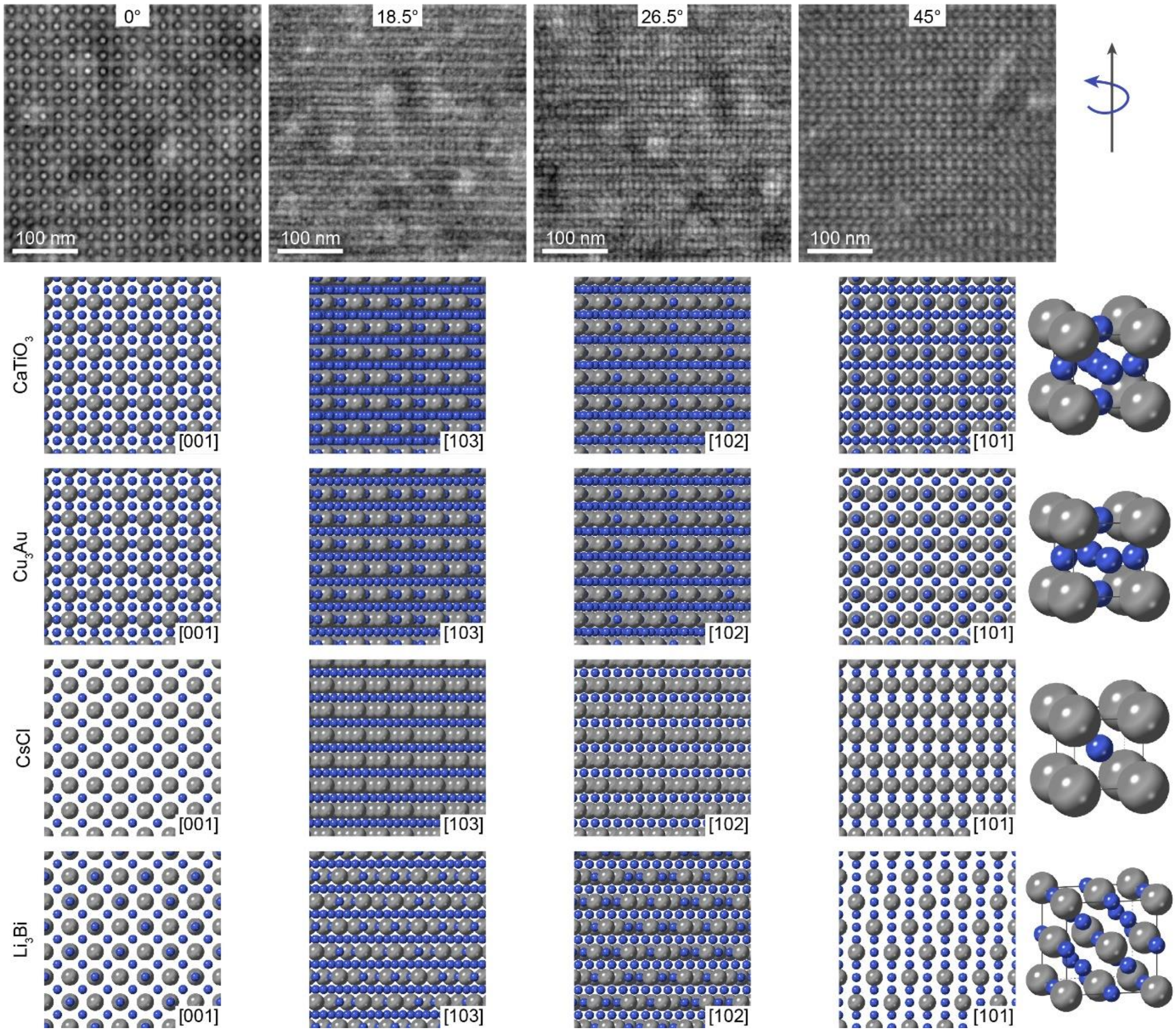


**Supplementary Fig. 8 | HAADF-STEM tilting series around the $[010]_{SL}$ axis for binary $ABO_3$-type SL comprising 8.6 nm $CsPbBr_3$ and 19.5 nm $Fe_3O_4$ NCs.** HAADF-STEM images of a SL domain at different tilting angles are compared with the corresponding projections of $CaTiO_3$, $Cu_3Au$, CsCl and $Li_3Bi$ structures.

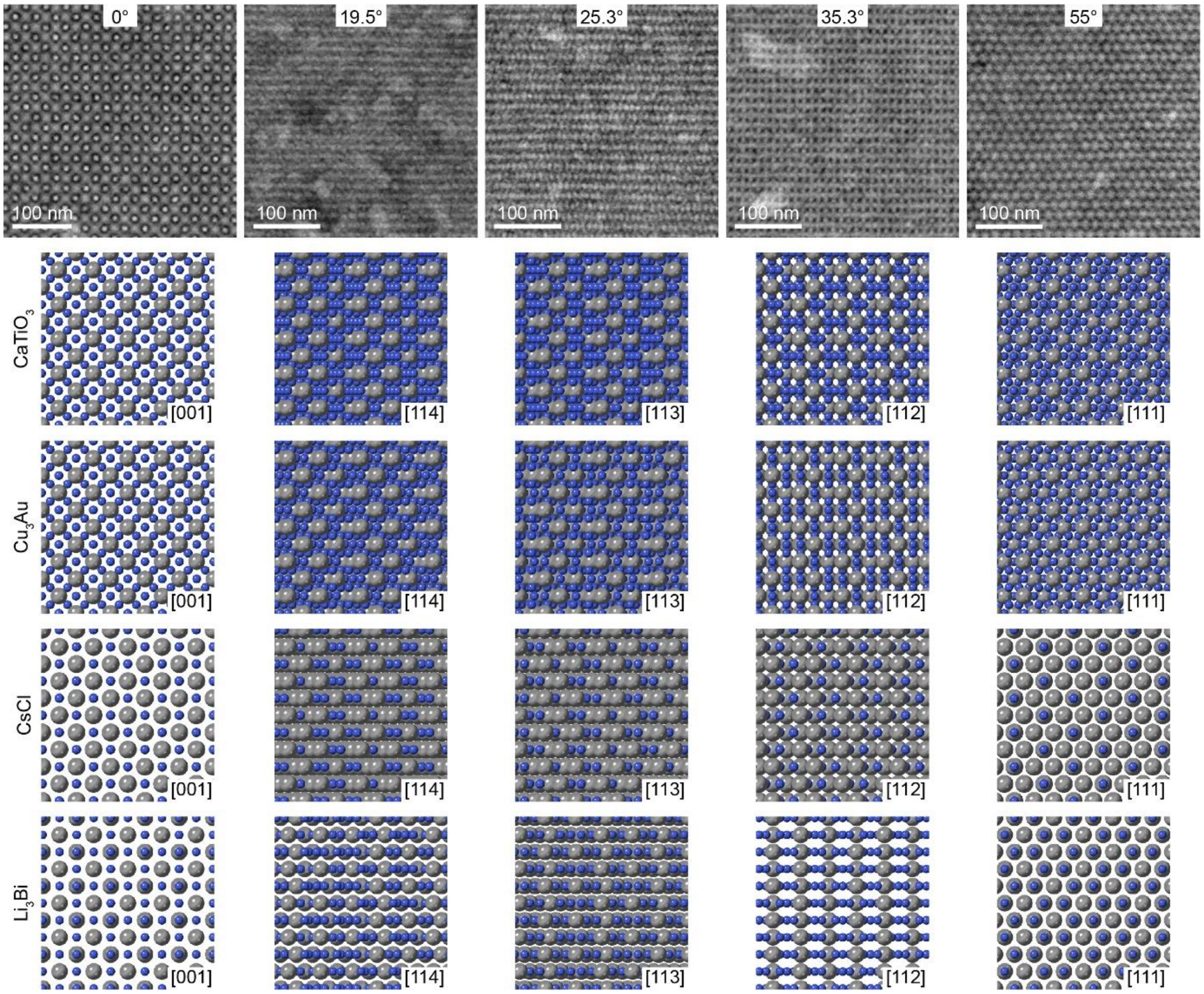


**Supplementary Fig. 9 | HAADF-STEM tilting series around the $[110]_{SL}$ axis for binary $ABO_3$-type SL comprising 8.6 nm $CsPbBr_3$ and 19.5 nm $Fe_3O_4$ NCs.** HAADF-STEM images of a SL domain at different tilting angles are compared with the corresponding projections of $CaTiO_3$, $Cu_3Au$, CsCl and $Li_3Bi$ structures.

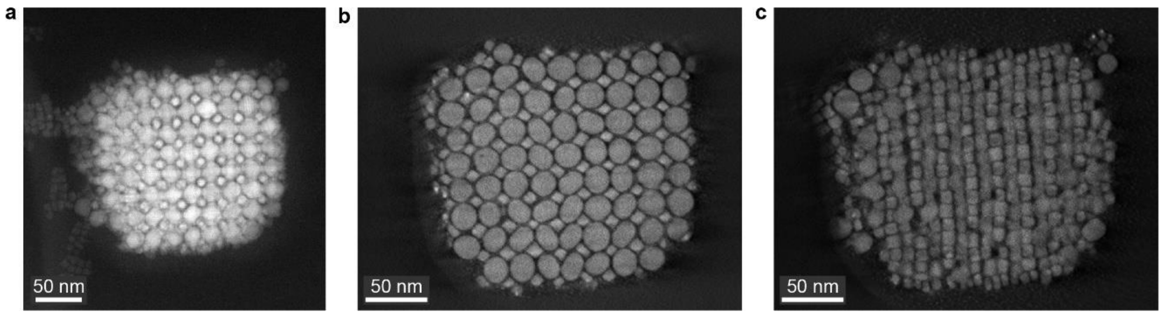


**Supplementary Fig. 10 | Tomographic reconstruction of binary $ABO_3$-type SL comprising 8.6 nm $CsPbBr_3$ and 19.5 nm $NaGdF_4$ NCs. a**, HAADF-STEM image of SL domain. **b**, Reconstruction of a volume slice through the $(001)_{SL}$ lattice plane confirms the orientation of O-site cubes that two of the <110> directions of $CsPbBr_3$ are aligned with $<100>_{SL}$. **c**, Reconstruction of a volume slice through the $(002)_{SL}$ lattice plane visualizes the orientation of B-site cubes (45° rotated compared to O-site cubes) with the <100> directions of $CsPbBr_3$ aligned with $<100>_{SL}$. See also Supplementary Video 1.

*8.6 nm $CsPbBr_3$ and 19.8 nm $Fe_3O_4$ – Binary $ABO_3$-type SL*

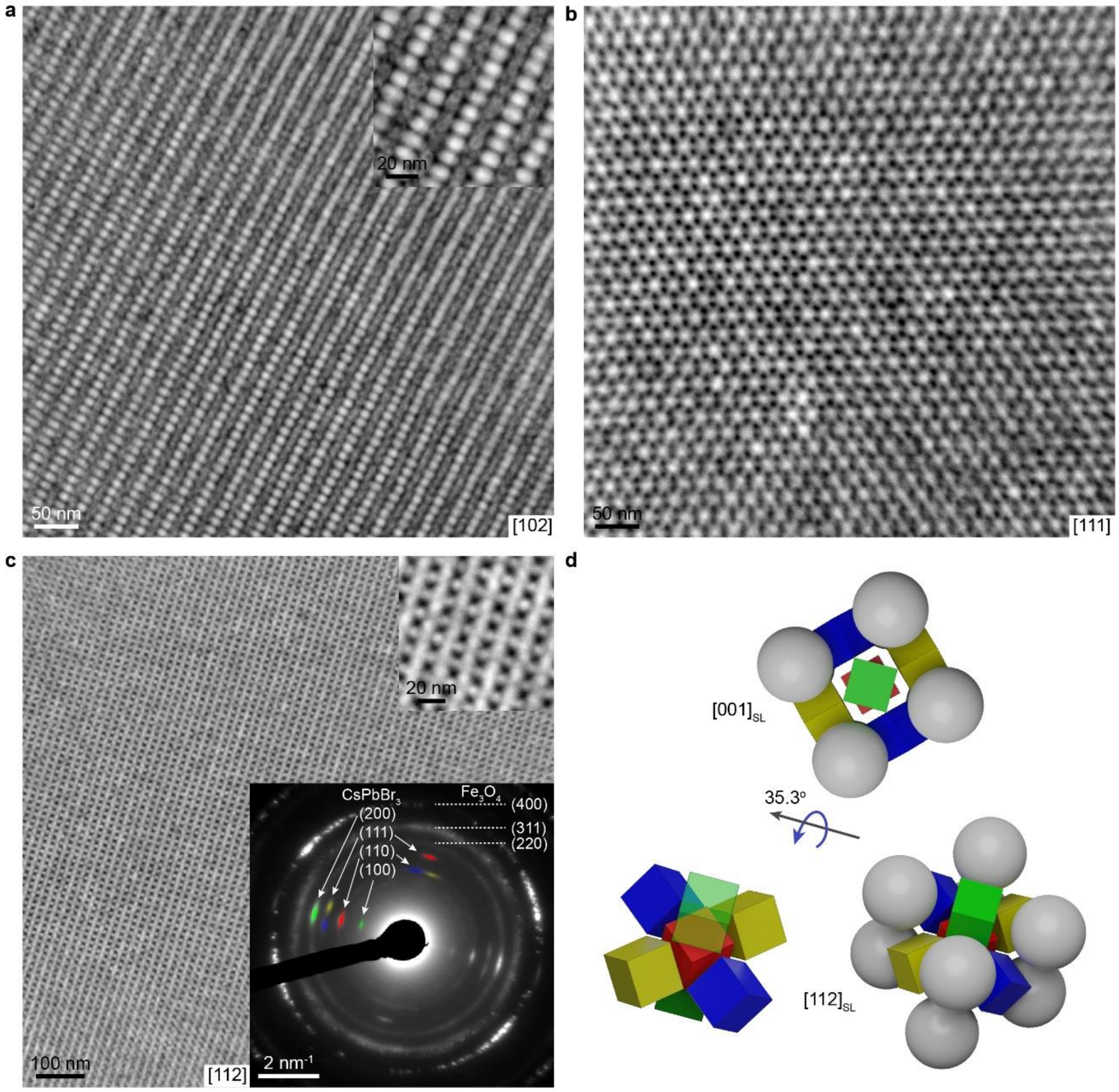


**Supplementary Fig. 11 | Binary $ABO_3$-type SL domains with different crystallographic orientations (8.6 nm $CsPbBr_3$ and 19.8 nm $Fe_3O_4$ NCs, $\gamma = 0.414$).** **a**, **b**, **c**, HAADF-STEM image in, respectively, $[102]_{SL}$, $[111]_{SL}$, $[112]_{SL}$ orientations. Upper insets show higher magnification images. The bottom inset in **c** shows the ED pattern from the single domain displayed in **c**. The origin of the $CsPbBr_3$ ED reflections is colour-coded to match the sketch **d**. **d**, Relationship between $[001]_{SL}$ and $[112]_{SL}$ projections in $ABO_3$ lattice. $[112]_{SL}$ projection can be obtained by a rotation of $[001]_{SL}$ projection around the $[110]_{SL}$ axis by ~35.3°. (111) reflection from a $CsPbBr_3$ nanocube located on B-site (centre of the unit cell) appears in ED pattern (marked in red) since in $[112]_{SL}$ projection (111) lattice planes of this cube become parallel to an electron beam. The presence of diffraction spots originating from (111) lattice planes of 3c nanocubes (blue and yellow) which are not parallel to the electron beam in the modeled structure (form 5.6° angle), may indicate a small deviation from the ideal cubic structure.

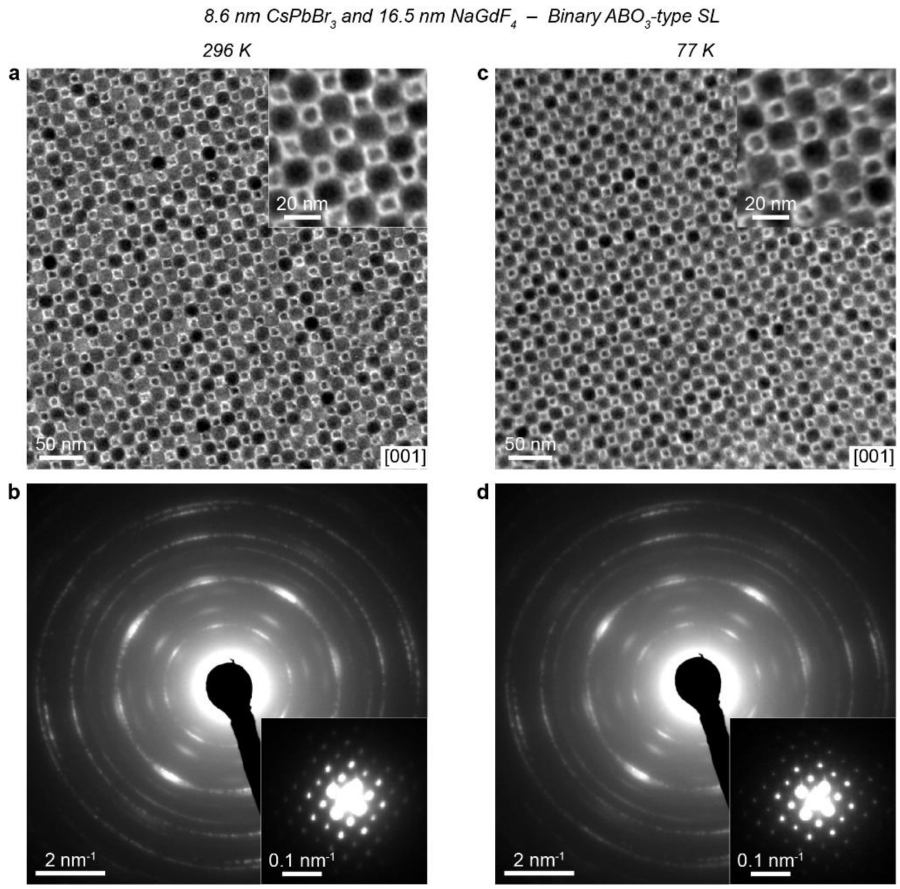


**Supplementary Fig. 12 | Cryo-TEM measurements of a binary $ABO_3$-type SL assembled from 8.6 nm $CsPbBr_3$ and 16.5 nm $NaGdF_4$ NCs on carbon-coated TEM grid. a**, TEM images and (**b**) corresponding wide- and small-angle (inset) ED patterns of a single SL domain in $[001]_{SL}$ orientation recorded at 296 K. **c**, TEM images and (**d**) corresponding wide- and small-angle (inset) ED patterns of the same domain recorded at 77 K.

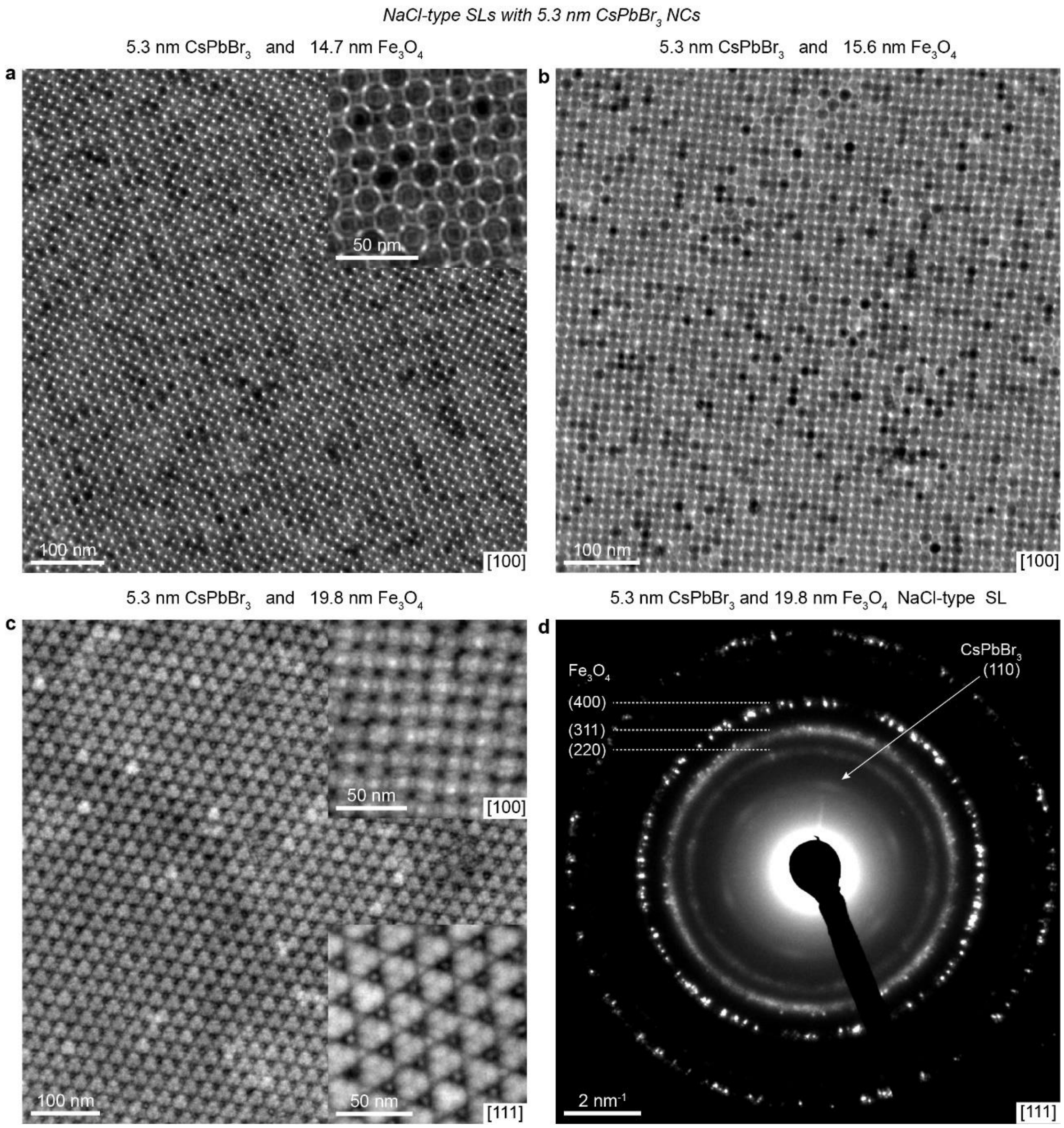


**Supplementary Fig. 13 | NaCl-type binary SLs from 5.3 nm $CsPbBr_3$ NCs combined with $Fe_3O_4$ NCs of different size.** **a**, TEM image of a SL domain in $[100]_{SL}$ orientation, $\gamma = 0.353$; top inset shows higher magnification image. **b**, TEM image of a SL domain in $[100]_{SL}$ orientation for $\gamma = 0.336$. **c**, HAADF-STEM image of a SL domain in $[111]_{SL}$ orientation for $\gamma = 0.274$; insets show higher magnification images in two typical orientations. **d**, ED pattern of a $[111]_{SL}$-oriented domain displayed in **c**. Splitting of $CsPbBr_3$ reflections from (111) lattice planes into six arcs indicates the loss of orientational freedom of nanocubes and alignment of <100> directions of $CsPbBr_3$ NCs with $<100>_{SL}$.

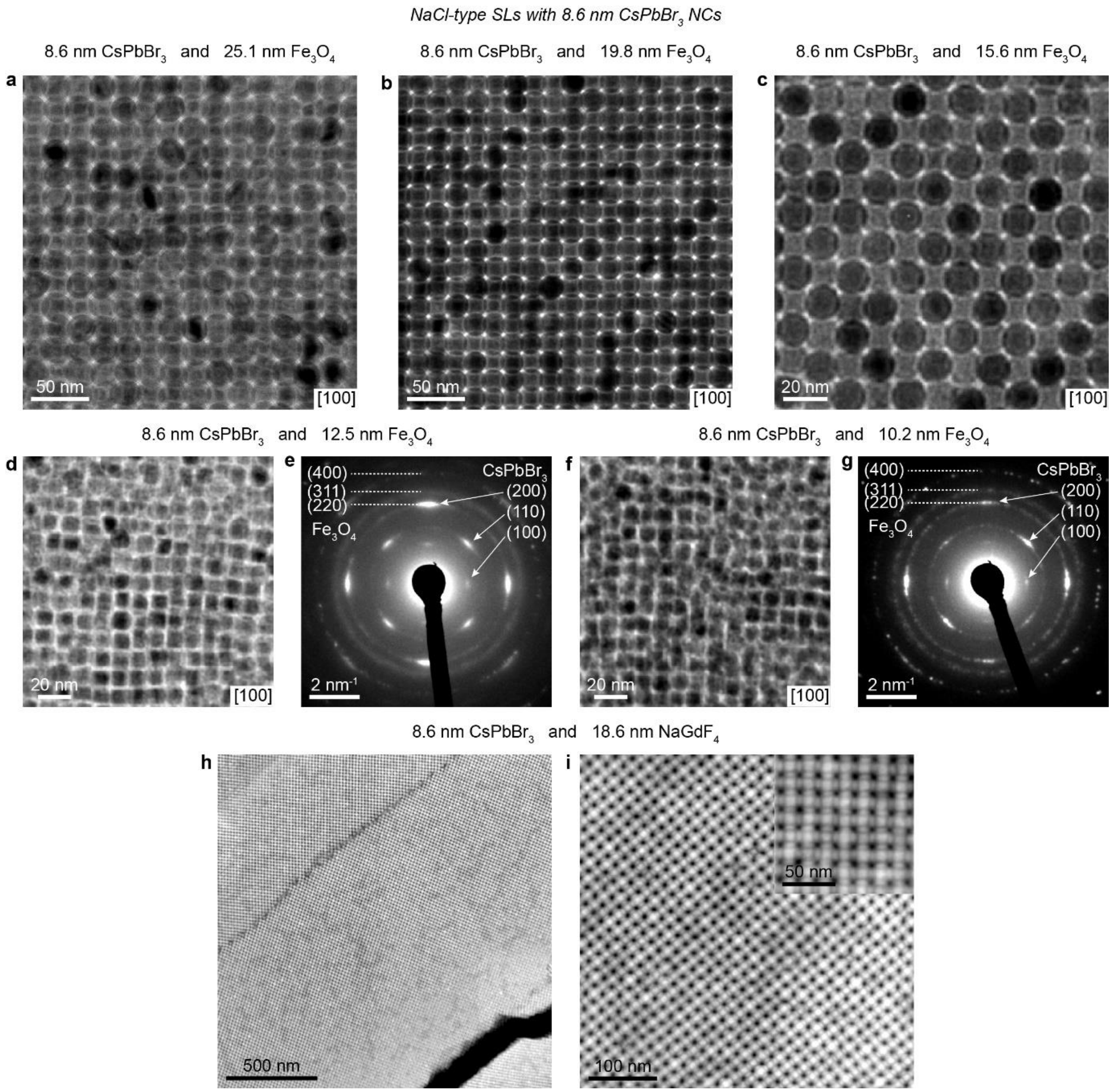


**Supplementary Fig. 14 | NaCl-type binary SLs from 8.6 nm $CsPbBr_3$ NCs combined with $Fe_3O_4$ and $NaGdF_4$ NCs of different size. a-c**, **d**, **f**, TEM images of binary SL domains in $[100]_{SL}$ orientation for $\gamma = 0.337$, $\gamma = 0.414$, $\gamma = 0.507$, $\gamma = 0.612$, $\gamma = 0.726$, respectively. **e, g**, ED patterns of SL domains displayed in **d** and **f**, respectively. **h, i**, HAADF-STEM images at a different magnification of a binary SL in $[100]_{SL}$ orientation assembled from 8.6 nm $CsPbBr_3$ and 18.6 nm $NaGdF_4$ NCs ($\gamma = 0.438$) on a $Si_3N_4$ membrane.

**References:**


58. Safko J. L., P. C., Goldstein H. *Classical Mechanics*. (Pearson, 2001).
59. Travesset, A. Phase diagram of power law and Lennard-Jones systems: crystal phases. *J. Chem. Phys.* **141**, 164501 (2014).
60. Anderson, J. A., Lorenz, C. D. & Travesset, A. General purpose molecular dynamics simulations fully implemented on graphics processing units. *J. Comput. Phys.* **227**, 5342-5359 (2008).
61. Glaser, J. *et al.* Strong scaling of general-purpose molecular dynamics simulations on GPUs. *Comput. Phys. Commun.* **192**, 97-107 (2015).
62. Anderson, J. A., Eric Irrgang, M. & Glotzer, S. C. Scalable Metropolis Monte Carlo for simulation of hard shapes. *Comput. Phys. Commun.* **204**, 21-30 (2016).
63. Travesset, A. Soft skyrmions, spontaneous valence and selection rules in nanoparticle superlattices. *ACS Nano* **11**, 5375-5382 (2017).
64. Ye, X., Chen, J. & Murray, C. B. Polymorphism in self-assembled $AB_6$ binary nanocrystal superlattices. *J. Am. Chem. Soc.* **133**, 2613-2620 (2011).
65. Travesset, A. Topological structure prediction in binary nanoparticle superlattices. *Soft Matter* **13**, 147-157 (2016).
66. Zha, X. & Travesset, A. The hard sphere diameter of nanocrystals (nanoparticles). *J. Chem. Phys.* **152**, 094502 (2020).
67. Landman, U. & Luedtke, W. D. Small is different: energetic, structural, thermal, and mechanical properties of passivated nanocluster assemblies. *Faraday Discuss.* **125**, 1-22 (2004).
68. Boles, M. A. & Talapin, D. V. Many-body effects in nanocrystal superlattices: departure from sphere packing explains stability of binary phases. *J. Am. Chem. Soc.* **137**, 4494-4502 (2015).
69. Linaburg, M. R., McClure, E. T., Majher, J. D. & Woodward, P. M. $Cs_{1-x}Rb_xPbCl_3$ and $Cs_{1-x}Rb_xPbBr_3$ solid solutions: understanding octahedral tilting in lead halide perovskites. *Chem. Mater.* **29**, 3507-3514 (2017).
70. Cottingham, P. & Brutchey, R. L. On the crystal structure of colloidally prepared $CsPbBr_3$ quantum dots. *Chem. Commun.* **52**, 5246-5249 (2016).
71. Bertolotti, F. *et al.* Crystal structure, morphology, and surface termination of cyan-emissive, six-monolayers-thick $CsPbBr_3$ nanoplatelets from X-ray total scattering. *ACS Nano* **13**, 14294-14307 (2019).
72. Bodnarchuk, M. I. *et al.* Rationalizing and controlling the surface structure and electronic passivation of cesium lead halide nanocrystals. *ACS Energy Lett.* **4**, 63-74 (2019).
73. Jun, Y. W., Lee, J. H., Choi, J. S. & Cheon, J. Symmetry-controlled colloidal nanocrystals: nonhydrolytic chemical synthesis and shape determining parameters. *J. Phys. Chem. B* **109**, 14795-14806 (2005).
74. Wang, Y. *et al.* Shape-controlled synthesis of PbS nanocrystals via a simple one-step process. *Langmuir* **28**, 16436-16443 (2012).
75. Smith, D. K., Goodfellow, B., Smilgies, D. M. & Korgel, B. A. Self-assembled simple hexagonal $AB_2$ binary nanocrystal superlattices: SEM, GISAXS, and defects. *J. Am. Chem. Soc.* **131**, 3281-3290 (2009).
76. Miyajima, K., Kagotani, Y., Saito, S., Ashida, M. & Itoh, T. Superfluorescent pulsed emission from biexcitons in an ensemble of semiconductor quantum dots. *J. Phys. Condens. Matter* **21**, 195802 (2009).
77. Ashner, M. N. *et al.* Size-dependent biexciton spectrum in $CsPbBr_3$ perovskite nanocrystals. *ACS Energy Lett.* **4**, 2639-2645 (2019).